

# The Fornax 3D project: PNe populations and stellar metallicity in edge-on galaxies

P. M. Galán-de Anta<sup>1,2\*</sup>, M. Sarzi<sup>1,3</sup>, T. W. Spriggs<sup>3\*\*</sup>, B. Nedelchev<sup>1,3</sup>, F. Pinna<sup>4</sup>, I. Martín-Navarro<sup>4,5,6</sup>, L. Coccato<sup>7</sup>, E. M. Corsini<sup>8,9</sup>, P. T. de Zeeuw<sup>10,11</sup>, J. Falcón-Barroso<sup>5,6</sup>, D. A. Gadotti<sup>7</sup>, E. Iodice<sup>12,7</sup>, R. J. J. Grand<sup>13</sup>, K. Fahrion<sup>7</sup>, M. Lyubenova<sup>7</sup>, R. M. McDermid<sup>14,15</sup>, L. Morelli<sup>16</sup>, G. van de Ven<sup>17</sup>, S. Viaene<sup>18</sup>, and L. Zhu<sup>19</sup>

<sup>1</sup> Armagh Observatory and Planetarium, College Hill, Armagh, BT61 9DG, UK

<sup>2</sup> Astrophysics Research centre, School of Mathematics and Physics, Queen's University Belfast, Belfast BT7 INN, UK

<sup>3</sup> Centre for Astrophysics Research, University of Hertfordshire, College Lane, Hatfield AL10 9AB, UK

<sup>4</sup> Max-Planck-Institut für Astronomie, Königstuhl 17, 69117 Heidelberg, Germany

<sup>5</sup> Instituto de Astrofísica de Canarias, Vía Láctea s/n, 38205 La Laguna, Tenerife, Spain

<sup>6</sup> Depto. Astrofísica, Universidad de La Laguna, Calle Astrofísico Francisco Sánchez s/n, 38206 La Laguna, Tenerife, Spain

<sup>7</sup> European Southern Observatory, Karl-Schwarzschild-Straße 2, 85748 Garching bei München, Germany

<sup>8</sup> Dipartimento di Fisica e Astronomia 'G. Galilei', Università di Padova, vicolo dell'Osservatorio 3, 35122 Padova, Italy

<sup>9</sup> INAF-Osservatorio Astronomico di Padova, vicolo dell'Osservatorio 5, 35122 Padova, Italy

<sup>10</sup> Sterrewacht Leiden, Leiden University, Postbus 9513, 2300 RA Leiden, The Netherlands

<sup>11</sup> Max-Planck-Institut fuer extraterrestrische Physik, Giessenbachstrasse, 85741 Garching bei Muenchen, Germany

<sup>12</sup> INAF - Astronomical Observatory of Capodimonte, Salita Moiariello 16, 80131, Naples, Italy

<sup>13</sup> Max-Planck-Institut für Astrophysik, Karl-Schwarzschild-Straße 1, 85748 Garching bei München, Germany

<sup>14</sup> Department of Physics and Astronomy, Macquarie University, Sydney, NSW 2109, Australia

<sup>15</sup> ARC Centre of Excellence for All Sky Astrophysics in 3 Dimensions (ASTRO 3D), Australia

<sup>16</sup> Instituto de Astronomía y Ciencias Planetarias, Universidad de Atacama, Avenida Copayapu 485, Copiapó, Chile

<sup>17</sup> Department of Astrophysics, University of Vienna, Türkenschanzstrasse 17, 1180 Vienna, Austria

<sup>18</sup> Sterrenkundig Observatorium, Universiteit Gent, Krijgslaan 281, 9000 Gent, Belgium

<sup>19</sup> Shanghai Astronomical Observatory, Chinese Academy of Sciences, 80 Nandan Road, Shanghai 200030, China

Received XXXXXX; accepted XXXXXX

## ABSTRACT

**Context.** Extragalactic Planetary Nebulae (PNe) are useful distance indicators and are often used to trace the dark-matter content in external galaxies. At the same time, PNe can also be used as probes of their host galaxy stellar populations and to help understanding the later stages of stellar evolution. Previous works have indicated that specific number of PNe per stellar luminosity can vary across different galaxies and as a function of stellar-population properties, for instance increasing with decreasing stellar metallicity.

**Aims.** In this study we further explore the importance of stellar metallicity in driving the properties of the PNe population in early-type galaxies, using three edge-on galaxies in the Fornax cluster offering a clear view into their predominantly metal-rich and metal-poor regions near the equatorial plane or both below and above it, respectively.

**Methods.** Using VLT-MUSE integral-field observations and dedicated PNe detection procedures, we construct the PNe luminosity function and compute the luminosity-specific number of PNe  $\alpha$  in both in- and off-plane regions of our edge-on systems.

**Results.** Comparing these  $\alpha$  values with metallicity measurements also based on the same MUSE data, we find no evidence for an increase in the specific abundance of PNe when transitioning between metal-rich and metal-poor regions.

**Conclusions.** Our analysis highlights the importance of ensuring spatial consistency to avoid misleading results when investigating the link between PNe and their parent stellar populations and suggest that in passively-evolving systems variations in the specific number of PNe may pertain to rather extreme metallicity regimes found either in the innermost or outermost regions of galaxies.

**Key words.** planetary nebulae: general – galaxies: abundances – galaxies: elliptical and lenticular, cD – techniques: imaging spectroscopy – methods: observational

## 1. Introduction

Planetary Nebulae can be detected in external galaxies out to great distances thanks to their intense [O III]  $\lambda 5007$  nebular emission, emitting as much as  $10^3 \sim 10^4 L_{\odot}$  (e.g. O'dell 1963; Paczynski 1970; Rose & Smith 1970; Gesicki et al. 2018). This makes PNe useful tracers for the kinematics of their parent stellar populations in the very outskirts of galaxies allowing to con-

strain their dark matter content (e.g. Romanowsky et al. 2003; Douglas et al. 2007; Coccato et al. 2009; Kafle et al. 2018). The PNe populations of external galaxies have also been found to have similar PN Luminosity Functions (PNLF) with a common bright-end cutoff that in turn makes PNe reliable cosmic distance indicators (Ciardullo et al. 1989; Ciardullo 2012).

As tracers of their parent stellar populations, extragalactic PNe can also help to understand the late stage of stellar evolution in galactic environments different from our Milky Way. In fact, both the detailed shape of the PNLF and the fact that

\* pgalandanta01@qub.ac.uk

\*\* tspriggs@outlook.com

PNe population in different kind of galaxies seems to share the same cutoff, are still not fully understood. For instance, the actual presence of bright PNe in old, passively evolving systems is a long-standing problem (Marigo et al. 2004; Ciardullo 2005) that only recent theoretical development has started to address (e.g. Gesicki et al. 2018; Valenzuela et al. 2019). Likewise, both the origin of the PNLF bright cut-off (e.g. Ciardullo 2012) and its slope at fainter regimes are not fully understood (e.g. in star-forming regions, as found in the LMC by Reid & Parker 2010 or in the outskirts of early-type galaxies, as shown by Hartke et al. (2020).

At a more basic level, the abundance of PNe should also vary across different kinds of galaxies, as proposed by Buzzoni et al. (2006, hereafter B06) also in relation to variations to their overall far-UV flux (the so-called UV-upturn, Burstein et al. 1988). In fact, B06 also showed the first observational evidence for an anti-correlation between the specific number of PNe per luminosity ( $\alpha$ ) and stellar metallicity, finding at the same time that the presence of a UV-upturn also corresponds to less abundant PNe populations (consistent also with previous theoretical work by Greggio & Renzini 1990). It is important to note, however, that the analysis of B06 suffers from a spatial inconsistency in their comparison of PNe and stellar population measurements. Indeed, whereas their  $\alpha$  values come from previous halo PNe studies (Ciardullo et al. 1989; Jacoby et al. 1989; Hui et al. 1993), their literature measurements for the Mgb index values (used to trace metallicity) and the UV-upturn pertain to the innermost regions of their sample galaxies.

Nowadays, deep imaging facilities allow us to trace radial variations in  $\alpha$  out to the most metal-poor halo regions of galaxies (e.g. Bhattacharya et al. 2019; Hartke et al. 2020). Furthermore, the advent of integral-field spectroscopy can both facilitate the measurement of the stellar metallicity in faint galaxy outskirts (by collecting large aperture spectra, e.g. Weijmans et al. 2009) and detection of PNe deeply embedded in the central bright regions of galaxies (thanks to a detailed spectral modelling, e.g. Sarzi et al. 2011; Pastorello et al. 2013; Spriggs et al. 2020), where they are otherwise inaccessible to narrow-band imaging or counter-dispersed slit-less spectroscopy (e.g. Gerhard et al. 2005; Douglas et al. 2007; Ventimiglia et al. 2011).

In this respect, edge-on galaxies can be considered as ideal laboratories to test ideas on the connection between PNe and their parent stellar populations. Indeed, the particular inclination of these galaxies makes it possible to directly compare PNe populations in metal-rich disc regions and their counterparts in the more metal-poor bulge or halo, thus allowing to start redressing the spatial inconsistencies in the B06 analysis.

Using MUSE integral-field spectroscopic data, in this paper we explore the PNe populations for the three edge-on galaxies FCC 153, FCC 170, and FCC 177. These targets were observed during the magnitude-limited Fornax3D survey for bright galaxies within the virial radius of the Fornax cluster (Sarzi et al. 2018). We place our findings in the context of the stellar population measurements previously reported by Pinna et al. (2019b,a, hereafter P19). These edge-on galaxies host a range of stellar populations that can be divided into a predominantly metal-rich bulge/thin-disc and a metal-poor off-plane populations. In this respect, PNe can be used to trace the kinematics of these parent stellar populations and check whether the abundance of hosted PNe is dependent on different star formation signatures such as the metallicity.

This paper is organised as follows. In Section 2, we present a brief summary of the sample galaxies as well as the properties of the observations. In Section 3, we explain the methodology and

**Table 1.** Point-spread function across the MUSE pointings of the sample galaxies, as characterised using a Moffat function fit to either a foreground star or a selection of bright PNe sources.

Galaxy	Method	Pointing	FWHM	$\beta$
(1)	(2)	(3)	(4)	(5)
FCC 153	PNe	Centre	3.6	1.9
		Halo	3.6	4.2
FCC 170	Star	Centre	4.1	2.4
		Halo	3.5	1.7
FCC 177	PNe	Centre	3.8	1.8
		Halo	4.1	4.4

**Notes.** (1) galaxy name. (2) selected object to estimate the PSF. (3) selected MUSE pointing. (4) FWHM values are in pixels. (5)  $\beta$  parameter of the Moffat profile. The values  $FWHM$  and  $\beta$  are taken from Spriggs et al. (in preparation).

procedures to identify and confirm the detected PNe, as well as to estimate the PNLF, light-weighted metallicity, and luminosity specific PNe number. In Section 4, we present and discuss the results of both the PNLF for the three galaxies and specific PNe number per galaxy as function of the metallicity of different in-plane and off-plane regions. Lastly, in Section 5 we give our conclusions.

## 2. Observations and data reduction

The MUSE data for FCC 153, FCC 170 and FCC 177 (IC 1963, NGC 1381, and NGC 1380A, respectively) were obtained in the wide-field mode, which ensures a spatial sampling of  $0.2'' \times 0.2''$  on a  $1' \times 1'$  field-of-view (FoV). The wavelength range of MUSE cubes ranges between 4650 Å and 9300 Å with a spectral sampling of  $1.25 \text{ \AA pixel}^{-1}$  and average instrumental spectral resolution of  $FWHM_{\text{int}} = 2.5 \text{ \AA}$  (Sarzi et al. 2018). In the particular case of our three edge-on galaxies, the MUSE data comprises of a central pointing and offset pointing further covering the outer disc and halo regions, and to which from now on we refer as the halo pointing. Different integration times of 1h and 1h30min for central and halo pointing, respectively, allow to reach the same limiting surface brightness of  $\mu_B = 25 \text{ mag arcsec}^{-2}$ . Central pointings were required to be observed under good seeing conditions ( $FWHM < 0.8''$ ), whereas halo pointings had less stringent image quality constraints ( $FWHM < 1.5''$ ). This will be accounted in our PNe analysis (see Section 3.2).

The data reduction was performed using the MUSE pipeline (Weilbacher et al. 2012) applying the ESOREFLEX environment (Freudling et al. 2013) as described in Sarzi et al. (2018) and Iodice et al. (2019). This includes key steps such as sky-subtraction, telluric correction and both relative and absolute flux calibration. Normally, the single pointings would be aligned through reference stars and further combined to produce final MUSE mosaics, but here this last step was skipped since our PNe analysis will need to be separately applied to our individual finally-reduced central and halo pointings due the aforementioned differences between their imaging quality.

Maps for the stellar kinematics of these objects were presented both in Pinna et al. (2019b,a) and in Iodice et al. (2019), with the former works additionally showed maps for the stel-

lar age and metallicity. These studies also noticed the absence of diffuse ionised-gas emission in these galaxies, although the presence of PNe in these and other passively-evolving objects was already being mentioned in Iodice et al. (2019). This is thanks to a careful spaxel-by-spaxel separation of the stellar continuum and nebular emission using the GandALF code (e.g. Sarzi et al. 2006) within the novel GIST pipeline of Bittner et al. (2019), as also described in Sarzi et al. (2018).

### 3. Methodology

In order to characterise the PNe populations of our edge-on galaxies we follow the method of Spriggs et al. (2020). This consists of five separate steps: i) identification of PNe candidate using [O III]  $\lambda 5007$  signal-to-noise maps obtained from our dedicated spaxel-by-spaxel GandALF fits, ii) dedicated 3D-fitting of such PNe candidates for their kinematics and total [O III]  $\lambda 5007$  flux while imposing a fixed spatial profile for their [O III]  $\lambda 5007$  emission according to the (pre-determined) spatial Moffat point-spread function (PSF)<sup>1</sup>, iii) isolating and removing PNe interlopers based on the comparison with the host-galaxy stellar kinematics and unresolved HII-regions or supernovae remnant PNe impostors using line diagnostics, iv) construction of the PNLF and of our PNe detection incompleteness function (Section 3.1) and v) finally, estimation of the total luminosity-specific number of PNe within a given magnitude limit (Section 3.2). This last step requires either adopting or deriving the galaxy distance using the PNLF, and involves re-scaling the incompleteness-corrected model for the PNLF to match the observed number of PNe.

The first three steps of this analysis deliver a catalogue for the PNe contained within the FoV of our MUSE observations. Separate PNe catalogues for each pointing are needed in first place since the central and halo data were obtained under rather different seeing conditions (Table 1), which impacts on the shape and extent of the incompleteness functions that we then fold in the PNLF modelling. Our detected PNe are in agreement with those in Spriggs et al. (in preparation), after that, the only difference is that here we will separately apply the last two steps of our PNe analysis to the predominantly metal-rich and metal-poor regions near and off the equatorial plane of our edge-on galaxies, respectively. We obtain separate PNLF and luminosity-specific PNe numbers in order to explore variations in the PNe populations of regions with significantly different parent stellar populations. For this we apply the stellar population differentiation adopted in Pinna et al. (2019a,b), which is shown by horizontal lines in the top panels of Figs. 1-3. Finally, using two complementary approaches we will proceed to estimate the stellar metallicity in these regions (Section 3.3) in order to place our PNe population results in the context of the B06 relation, which we will also re-evaluate using the stellar metallicity measurements from the literature (Section 3.4).

#### 3.1. Observed PNLF, completeness corrections and best-matched PNLF models

Following the procedure outlined in the previous section we obtain separate catalogues for PNe populations encompassed by

<sup>1</sup> The PSF evaluation assumes a Moffat (1969) profile and is achieved using foreground stars by simultaneously applying our 3D-fitting procedure to the [O III]  $\lambda 5007$  emission of a few bright PNe. The radial extent and kurtosis of the Moffat profile is defined by its parameters  $\alpha$  and  $\beta$ , which relate to the FWHM =  $2\alpha\sqrt{2^{1/\beta}-1}$ .

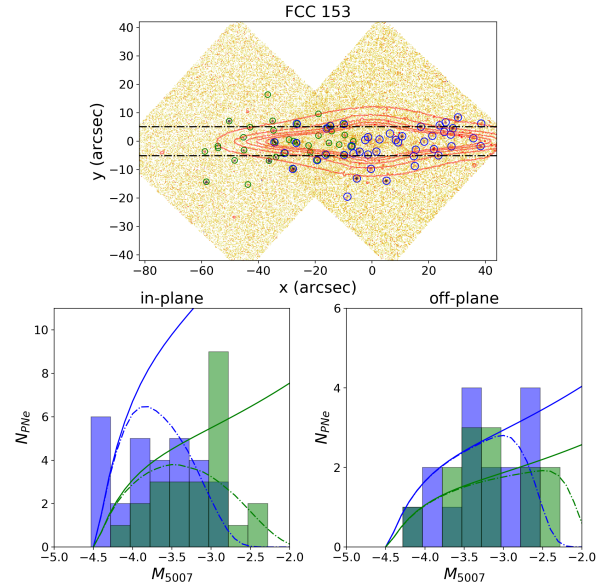


**Fig. 1.** PNLF of FCC 153 for in-plane and off-plane regions. *Top panel:* map of the [O III]  $\lambda 5007$  line. The blue circles represent the detected PNe in central pointing whereas the green ones show the detected objects in the halo pointing. The black dashed lines indicate the separation between in-plane and off-plane regions. *Bottom panels:* PNLF of both components: in-plane (left panel) and off-plane (right panel). The blue histograms as well as the blue solid and dashed lines represent the PNLF for PNe in the central pointing, whereas the green histograms along with the green solid and dashed lines indicate the PNLF for the PNe in the halo pointing. The red contours are the isophotes of the flux white image.

our central and halo MUSE pointings. The location of our detected PNe is shown in the top panels of Figs. 1-3 for each galaxy, with blue and green circles for PNe identified in the central and halo pointing, respectively. We then further divide the central and halo PNe in two sub-catalogues for regions close to the equatorial plane and those lying above and below it, and construct corresponding PNe luminosity functions as shown in the lower panels of Figs. 1-3. To first order, after accounting for the incompleteness of our observations, adjusting for distance and applying an appropriate re-scaling, our observed PNLF should compare well with the standard form of the PNLF function introduced by Ciardullo et al. (1989). This is given by

$$N(M) \propto e^{0.307M_{5007}} \left[ 1 - e^{3(M_{5007}^* - M_{5007})} \right], \quad (1)$$

where  $M_{5007}^* = -4.52$  mag is the characteristic bright-end cut-off (according to the latest calibration of Ciardullo 2012) that makes the PNLF a useful distance indicator.

Following Spriggs et al. (2020) we define the PNe detection completeness at a given apparent magnitude  $m_{5007}$  as the fraction of galaxy stellar light within the MUSE FoV where a PNe of that particular magnitude can be detected. For this, we apply our PNe detection criteria on a spaxel-by-spaxel basis, by first computing the peak [O III]  $\lambda 5007$  flux for PNe of apparent magnitude  $m_{5007}$  (given our PSF model) and subsequently checking if the corresponding peak  $A_{[\text{O III}]}$  spectral amplitude (given the MUSE spectral resolution and the typical PNe intrinsic  $\sigma$  of  $\sim 40$  km s<sup>-1</sup>) exceeds three times the local residual-noise level from our previous spaxel-by-spaxel GandALF spectral fitting.

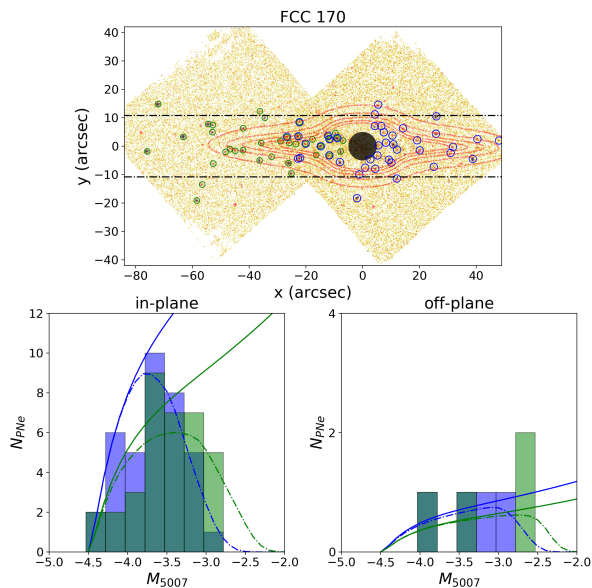


**Fig. 2.** Same as Fig. 1, but for FCC 170. The black circular area corresponds to the excluded template mismatch region.

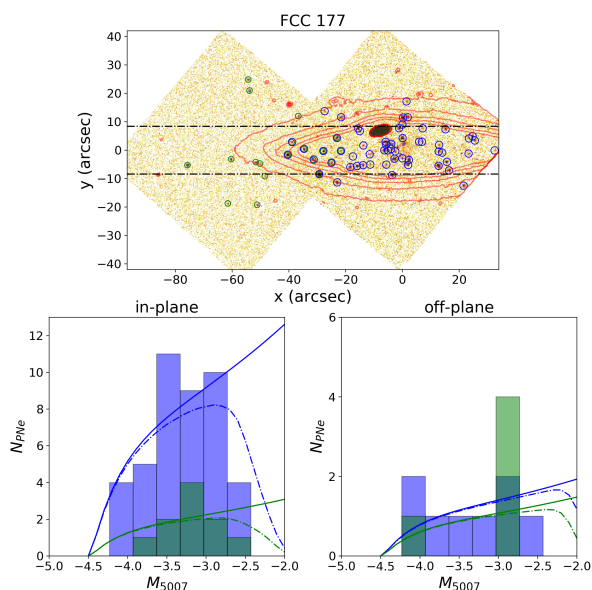


**Fig. 3.** Same as Figs. 1, but for FCC 177. The black elliptical area corresponds to the excluded foreground galaxy.

This procedure is equivalent to randomly populating the MUSE FoV with simulated PNe of magnitude  $m_{5007}$  while considering that larger numbers would be expected in brighter regions, and then simply evaluate the completeness as the fraction of PNe that would be detected (see also Sarzi et al. 2011; Pastorello et al. 2013). During this procedure we also exclude regions affected by either background or foreground sources (e.g. in FCC 177) and where we have evidence of significant systematic effects in our spectral fitting (i.e. template-mismatch during

the spaxel-by-spaxel GandALF fit) that would lead to spurious PNe detection or biased [OIII] flux measurements (e.g. in the central regions of FCC 170).

The outlined procedure is separately applied to the in and off-plane regions in both central and halo pointings to construct the PNLFs shown in Figs. 1-3.

With these completeness-correction functions at hand, we first consider the best distance to our sample objects from Spriggs et al. (in preparation), using all the data from the central pointing, where the seeing conditions are less prominent. In short, this procedure adjusts the distance modulus until the observed cumulative PNLF distribution is optimally matched by the corresponding distance-shifted and completeness-corrected cumulative Ciardullo PNLF, through a minimisation of the Kolgorov-Smirnov statistics. Once this best distance is obtained, we compute appropriately shifted and completeness-corrected model PNLF for each of the in- and off- plane regions in the central and halo pointing, further rescaling them until their integrated value matches the total number of PNe observed in these regions. Such adjusted model PNLFs are also shown in the lower panels of Figs. 1-3, and are based on best-fitting distances of 21.7, 19.6 and 17.8 Mpc for FCC153, FCC170 and FCC177, respectively (Spriggs et al. in preparation). As detailed in that paper, these distances are in good agreement with other measurements, such as those based on surface brightness fluctuations as in Blakeslee et al. (2009).

### 3.2. Total and Luminosity-specific PNe numbers

Once the Ciardullo et al. (1989) PNLF has been matched to the observed PNLF in the in- and off-plane regions of our edge-on galaxies, we can estimate the total number of PNe from the bright cut-off down to a chosen magnitude limit by simply integrating the shifted and re-scaled model PNLF as it is. Following Buzzoni et al. (2006), in this way we estimate the true number  $N_{2.5}$  of PNe 2.5 magnitude from the PNLF bright cut-off. To this extrapolated total, we associate errors obtained from appropriately rescaling the Poisson uncertainty on the the actual number of PNe that we observe within a given region, computed following the prescription of Gehrels (1986).

From this number, we can estimate the so-called luminosity specific number of PNe

$$\alpha_{2.5} = \frac{N_{2.5}}{L_{bol}}, \quad (2)$$

where  $L_{bol}$  is the bolometric luminosity for the region where we have been looking for PNe. In turn this is given by

$$L_{bol}(L_{\odot}) = 10^{-0.4(M_{\lambda} - M_{\lambda,\odot})} \times 10^{-0.4(BC_{\lambda} - BC_{\lambda,\odot})}, \quad (3)$$

where  $M_{\lambda}$  and  $M_{\lambda,\odot}$  are the absolute magnitude for the region of interest within the galaxy and the Sun within a chosen broad-band filter, while  $BC_{\lambda}$  and  $BC_{\lambda,\odot}$  are the corresponding bolometric magnitude corrections from the given broad-band filter. See also Torres (2010, Eq. 9) and Hartke et al. (2020, Eq. 14).

In the case of our MUSE observations, we have chosen the SDSS  $g$ -band to compute the observed  $m_g$  and absolute  $M_g$  magnitude of the in and off-plane regions in our edge-on galaxies. As for deriving the bolometric correction, we follow the procedure described by Spriggs et al. (2020) whereby  $BC_g$  is derived using the optimal combination of EMILES stellar templates (Vazdekis et al. 2016) that best matches the MUSE integrated spectrum observed within the region of interest (i.e. our in and off-plane region in both central and halo pointing). Adopting a bolometric

correction for the Sun in the  $g$ -band of  $BC_{g,\odot} = -1.78$  mag and a  $g$ -band absolute magnitude of  $M_{g,\odot} = 5.23$  mag (Willmer 2018), and using Eq. (3), we estimate the bolometric luminosity of our in and off plane regions, which are reported in Table 2. Errors in  $L_{bol}$  are dominated by  $M_{\lambda}$  errors from distance uncertainties.

### 3.3. Stellar metallicity measurements from integrated MUSE spectra

In order to place our PNe findings in relation to the properties of their parent stellar population and in particular to check on any dependence of  $\alpha_{2.5}$  with stellar metallicity, we proceed to measure the latter in both the in and off-plane regions in and above the disc of our edge-on galaxies, both in MUSE central and halo pointings. For this, we integrate our MUSE spectra in these regions (as defined by P19; Section 3) over a minimum signal-to-noise of 1, obtaining 4 different spectra for each galaxy, and we derive the stellar metallicity according to the following two approaches:

- Full spectral fitting using the pPXF code (Cappellari & Emsellem 2004; Cappellari 2017) in the 4750-5500 Å wavelength range as done in P19, using a set of single-age stellar population spectral models from the MILES library (Falcón-Barroso et al. 2011) to estimate an average value for the stellar metallicity.
- Spectral fitting focused on the wavelength regions around a specific set of absorption-line features particularly sensitive to either age (e.g.  $H_{\beta}$ ), metallicity (e.g. Fe 5270, Fe 5335, etc.) or  $\alpha$ -element abundance (e.g. Mg 5177) as done in Martín-Navarro et al. (2019) using also the single-age stellar population models from the MILES library to derive a single, best-fitting value for the metallicity  $[Z/H]_{SSP}$ .

These two methods are complementary. The spectral-fitting approach of P19 allows to account for an extended star-formation and metal-enrichment history through a combination of single-age models of varying age and metallicity instead of adopting only the values corresponding to the best matching single-age stellar population model as in Martín-Navarro et al. (2019). The latter approach however also accounts for more subtle variations in  $\alpha$ -element abundances (and in fact, also in the slope at the low-mass-end of the stellar initial-mass function), to which full-spectral fitting can be rather insensitive<sup>2</sup>.

### 3.4. Revising the Buzzoni et al. relation

The evidence for the anti-correlation between the specific number of PNe  $\alpha_{2.5}$  and stellar metallicity of B06 was based on literature measurements for the strength of the  $Mg_2$  absorption-line index rather than an actual metallicity measurement. To quantify the  $\alpha_{2.5}$  variations that they would have found with actual metallicity measurements, we took all the objects in B06 sample that were also observed over the course of the ATLAS<sup>3D</sup> survey (Cappellari et al. 2011). Using the measurements of McDermid et al. (2015) we revisit the  $\alpha_{2.5}$ -metallicity relation of B06. As in the case of our two adopted approaches to estimate the stellar metallicity, McDermid et al. (2015) provide average (light-weighted) values based on full-spectral fitting  $[Z/H]_{SFH}$

<sup>2</sup> Whereas P19 derived mass-weighted values here we use instead light-weighted averages  $[Z/H]_{SFH}$  in order to be more consistent with the approach of Martín-Navarro et al. Our conclusions are not affected by this choice.

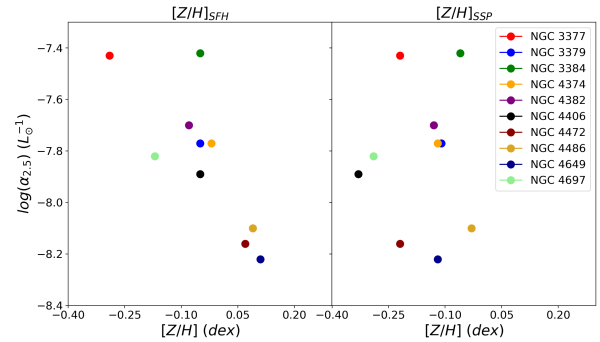


**Fig. 4.** PNe specific number vs stellar metallicity for Buzzoni et al. (2006) sample galaxies covered also by the ATLAS<sup>3D</sup> integral-field spectroscopic survey (see McDermid et al. 2015), for two different star-formation history measurements: full spectral fitting from a single-age stellar population (*left panel*) and full-index-fitting based on a focused set of absorption lines (*right panel*).

and single-age values from the best stellar-population model  $[Z/H]_{SSP}$  that best matched the observed strength of a set of absorption line-strength indices, while accounting for  $[\alpha/Fe]$  variations.

Fig. 4 shows that such a revised  $\alpha_{2.5}$  - metallicity relation remains in place only when considering  $[Z/H]_{SFH}$  values, indicating at best a factor  $\sim 6$  variation in the specific number of PNe per 0.4 dex variation in metallicity. No visible trend is present when considering  $[Z/H]_{SSP}$  values. This suggests that either  $[\alpha/Fe]$  may also play a part in the original trend with the  $Mg_2$  line-strength index (which subsists also when looking at the ATLAS<sup>3D</sup>  $Mg_b$  values) or caution is needed when considering the widely different spatial scales probed by B06.

## 4. Results and discussion

Given our final estimates for the specific number of PNe 2.5 magnitudes from the PNLF bright cut-off and stellar metallicity in the regions near or above and below the equatorial plane of our sample galaxies (Table 2), Fig. 5 finally shows how these quantities fare against each other across such different regions and as observed both in our central and halo MUSE pointings.

We observe no significant difference in  $\alpha_{2.5}$  between in and off-plane regions, irrespective of the methodology used to estimate the stellar metallicity, finding at most a factor  $\sim 2.6$  increase in  $\alpha_{2.5}$  between the off-plane measurements of FCC 177 where there is a 0.33 dex difference. This lack of a trend appears to contradict the results of B06. Indeed, even though the metallicity estimates for the predominantly metal-poor off-plane regions can span a wide range of values, on average they are  $\sim 0.4$  dex lower than their counter parts closer to the equatorial plane and therefore ought to show up to  $\sim 6$  times higher values for  $\alpha_{2.5}$  according to our most optimistic revision of the B06 analysis (Section 3.4). Despite the large uncertainties in the  $\alpha_{2.5}$  values for such fainter off-plane regions, there simply is no room to accommodate a factor 6 (i.e.  $\sim 0.8$  dex) increase in  $\log(\alpha_{2.5})$ .

This result is at odds with the recent work of Hartke et al. (2020), who find a clear increase in the specific PNe number in the outskirts of the closer Leo Group early-type galaxy NGC 3379 (M105), based on deep narrow-band on-off imaging extending out to nearly 23 effective radii ( $R_e$ ). This study reveals, however, that such an enhancement in  $\alpha$  values begins from  $8R_e$  onward, deep in the outer stellar halo or even in the intra-group

**Table 2.** Results of the analysis for the MUSE central and halo pointings of the sample galaxies.

Galaxy (1)	Region (2)	PNe detected per region (3)	$N_{2.5}$ (4)	$L_{bol}$ ( $L_{\odot}$ ) (5)	$\alpha_{2.5}$ ( $L_{\odot}^{-1}$ ) (6)	$[Z/H]_{SSP}$ (dex) (7)	$[Z/H]_{SFH}$ (dex) (8)
Central pointing							
FCC 153	in-plane	29	$99^{+22}_{-18}$	$(4.7^{+0.7}_{-0.5}) \times 10^9$	$(2.1^{+0.5}_{-0.4}) \times 10^{-8}$	-0.13	0.008
	off-plane	16	$24^{+8}_{-6}$	$(1.2^{+0.2}_{-0.1}) \times 10^9$	$(2.0^{+0.6}_{-0.5}) \times 10^{-8}$	-0.645	-0.617
FCC 170	in-plane	38	$116^{+22}_{-19}$	$(5.7^{+0.7}_{-0.6}) \times 10^9$	$(2.0^{+0.4}_{-0.4}) \times 10^{-8}$	-0.188	-0.11
	off-plane	4	$7^{+6}_{-3}$	$(6.3^{+0.8}_{-0.7}) \times 10^8$	$(1.1^{+0.6}_{-0.7}) \times 10^{-8}$	-0.595	-0.63
FCC 177	in-plane	46	$62^{+11}_{-9}$	$(2.6^{+0.5}_{-0.4}) \times 10^9$	$(2.4^{+0.5}_{-0.6}) \times 10^{-8}$	-0.173	-0.057
	off-plane	10	$9^{+4}_{-3}$	$(5.8^{+1.1}_{-0.9}) \times 10^8$	$(1.5^{+1.8}_{-1.8}) \times 10^{-8}$	-0.135	-0.556
Halo pointing							
FCC 153	in-plane	24	$45^{+11}_{-9}$	$(1.9^{+0.3}_{-0.2}) \times 10^9$	$(2.3^{+0.6}_{-0.5}) \times 10^{-8}$	-0.049	0.016
	off-plane	14	$15^{+5}_{-4}$	$(5.7^{+0.8}_{-0.6}) \times 10^8$	$(2.6^{+0.8}_{-0.7}) \times 10^{-8}$	-0.554	-0.483
FCC 170	in-plane	35	$76^{+15}_{-13}$	$(2.6^{+0.3}_{-0.3}) \times 10^9$	$(2.9^{+0.6}_{-0.6}) \times 10^{-8}$	-0.51	-0.07
	off-plane	4	$5^{+4}_{-3}$	$(2.0^{+0.3}_{-0.2}) \times 10^{-8}$	$(2.5^{+1.5}_{-1.6}) \times 10^{-8}$	-0.048	0.32
FCC 177	in-plane	12	$15^{+6}_{-4}$	$(5.8^{+1.1}_{-0.9}) \times 10^8$	$(2.6^{+0.8}_{-0.8}) \times 10^{-8}$	-0.158	-0.168
	off-plane	7	$7^{+4}_{-3}$	$(1.8^{+0.3}_{-0.3}) \times 10^8$	$(3.9^{+1.8}_{-1.8}) \times 10^{-8}$	-0.47	-0.894

**Notes.** (1) target galaxy. (2) studied region. (3) number of observed PNe. (4) theoretical expected number of PNe down to 2.5 magnitudes. (5) bolometric luminosity. (6) luminosity specific PNe number. (7) light-weighted metallicity derived from SSP index measurements. (8) light-weighted metallicity obtained from the analysis of full spectral fitting.

light medium and at metallicity regime most likely below the one found in the metal-poor extra-planar regions of our edge-on galaxies. On the other hand, at smaller radii Hartke et al. (2020) find no  $\alpha$  variation despite the presence of large stellar population gradients (e.g. within 3–4  $R_e$ , Weijmans et al. 2009) and this is consistent with our findings. Changing perspective, the lack of a trend between  $\alpha$  and metallicity contrasts also with the decrease in the number of bright post-AGB stars and increase in the far-UV flux towards the nuclear metal-rich regions of M31 found by Rosenfield et al. (2012), and corresponds to tentative evidence for a decrease in the number of bright PNe (Pastorello et al. 2013). Although edge-on systems are not particularly suited to explore the innermost and crowded PNe populations of galaxies, future MUSE studies assisted by adaptive optics have the potential to shed more light in this respect.

## 5. Conclusions

Using MUSE observations, we have explored the PNe populations in three edge-on galaxies in the Fornax cluster, offering an unique benchmark for testing the presence of systematic differences in the PNe content between predominantly metal-rich regions near the equatorial plane and generally metal-poor off-plane populations. We have found no significant evidence of a change in the specific number of PNe between the metal-poor and metal-rich regions of our edge-on galaxies, despite us probing a range in stellar metallicity values (0.5 dex) similar to that

of previous investigations which were however comparing the properties of PNe and their parent stellar population on rather different spatial scales. Presently, our results further suggest that variations in the specific number of PNe in passively-evolving systems may pertain either to extreme metallicity regimes and to the innermost or outermost regions of galaxies.

*Acknowledgements.* This work was supported by Science and Technology Facilities Council [grant number ST/R504786/1]. We really appreciate the computational facilities provided by University of Hertfordshire and Swinburne University to provide us with the necessary storage and analysis of the MUSE data, necessary to carry out our analysis. F.P., I. M-N, and J. F-B acknowledge support through the RAVET project by the grant PID2019-107427GB-C32 from the Spanish Ministry of Science, Innovation and Universities (MCIU), and through the IAC project TRACES which is partially supported through the state budget and the regional budget of the Consejería de Economía, Industria, Comercio y Conocimiento of the Canary Islands Autonomous Community. EMC acknowledges support by Padua University grants DOR1885254/18, DOR1935272/19, and DOR2013080/20 and by MIUR grant PRIN 2017 20173ML3WW\_01.GvdV acknowledges funding from the European Research Council (ERC) under the European Union’s Horizon 2020 research and innovation programme under grant agreement No 724857 (Consolidator Grant ArcheoDyn).

## References

- Bhattacharya, S., Arnaboldi, M., Hartke, J., et al. 2019, A&A, 624, A132  
 Bittner, A., Falcón-Barroso, J., Nedelchev, B., et al. 2019, A&A, 628, A117  
 Blakeslee, J. P., Jordán, A., Mei, S., et al. 2009, ApJ, 694, 556  
 Burstein, D., Bertola, F., Buson, L. M., Faber, S. M., & Lauer, T. R. 1988, ApJ, 328, 440

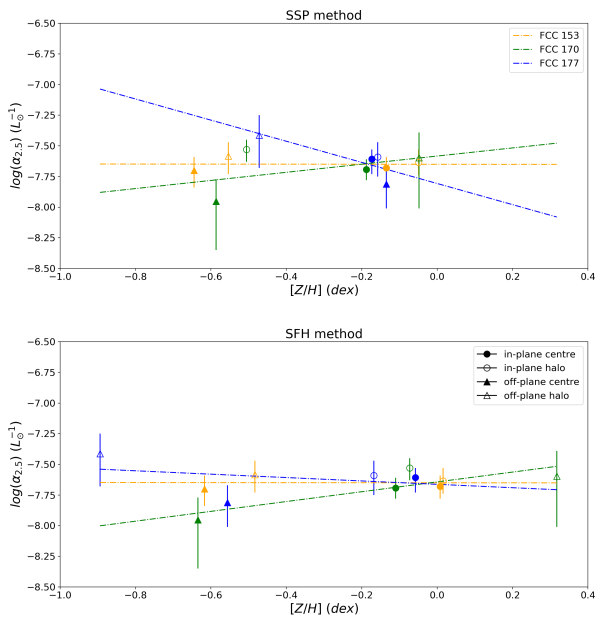


**Fig. 5.** Luminosity specific PNe number  $\alpha$  as a function of metallicity for the best-fitting single-age stellar population to selected spectral regions (top panel) following Martín-Navarro et al. (2019) and for the light-weighted metallicity resulting from a full spectral fitting (bottom panel) following P19. Circles and triangles show values from in-plane and off-plane regions, respectively whereas filled and open symbols denote whether these were found within our central or halo MUSE pointings. The colour of the symbols indicate measurements from each galaxy, with dashed lines showing linear fits to all values for each object.

Buzzoni, A., Arnaboldi, M., & Corradi, R. L. M. 2006, *MNRAS*, 368, 877  
 Cappellari, M. 2017, *MNRAS*, 466, 798  
 Cappellari, M. & Emsellem, E. 2004, *Publications of the Astronomical Society of the Pacific*, 116, 138  
 Cappellari, M., Emsellem, E., Krajnović, D., et al. 2011, *MNRAS*, 416, 1680  
 Ciardullo, R. 2005, in *American Institute of Physics Conference Series*, Vol. 804, *Planetary Nebulae as Astronomical Tools*, ed. R. Szczerba, G. Stasińska, & S. K. Gorny, 277–283  
 Ciardullo, R. 2012, *Ap&SS*, 341, 151  
 Ciardullo, R., Jacoby, G. H., Ford, H. C., & Neill, J. D. 1989, *ApJ*, 339, 53  
 Coccato, L., Gerhard, O., Arnaboldi, M., et al. 2009, *MNRAS*, 394, 1249  
 Douglas, N. G., Napolitano, N., Romanowsky, A. J., et al. 2007, *The Astrophysical Journal*, 664, 257  
 Falcón-Barroso, J., Sánchez-Blázquez, P., Vazdekis, A., et al. 2011, *A&A*, 532, A95  
 Freudling, W., Romaniello, M., Bramich, D. M., et al. 2013, *A&A*, 559, A96  
 Gehrels, N. 1986, *ApJ*, 303, 336  
 Gerhard, O., Arnaboldi, M., Freeman, K. C., et al. 2005, *ApJ*, 621, L93  
 Gesicki, K., Zijlstra, A. A., & Miller Bertolami, M. M. 2018, *Nature Astronomy*, 2, 580  
 Greggio, L. & Renzini, A. 1990, in *Astrophysics and Space Science Library*, Vol. 160, *Windows on Galaxies*, ed. G. Fabbiano, J. S. Gallagher, & A. Renzini, 63  
 Hartke, J., Arnaboldi, M., Gerhard, O., et al. 2020, *arXiv e-prints*, arXiv:2008.01696  
 Hui, X., Ford, H. C., Ciardullo, R., & Jacoby, G. H. 1993, *ApJ*, 414, 463  
 Iodice, E., Sarzi, M., Bittner, A., et al. 2019, *A&A*, 627, A136  
 Jacoby, G. H., Ciardullo, R., Ford, H. C., & Booth, J. 1989, *ApJ*, 344, 704  
 Kafle, P. R., Sharma, S., Lewis, G. F., Robotham, A. S., & Driver, S. P. 2018, *Monthly Notices of the Royal Astronomical Society*, 475, 4043  
 Marigo, P., Girardi, L., Weiss, A., Groenewegen, M. A. T., & Chiosi, C. 2004, *A&A*, 423, 995  
 Martín-Navarro, I., Lyubenova, M., van de Ven, G., et al. 2019, *A&A*, 626, A124  
 McDermid, R. M., Alatalo, K., Blitz, L., et al. 2015, *MNRAS*, 448, 3484  
 Moffat, A. 1969, *Astronomy and Astrophysics*, 3, 455  
 O’dell, C. 1963, *The Astrophysical Journal*, 138, 67  
 Paczynski, B. 1970, *Acta Astronomica*, 20, 47  
 Pastorello, N., Sarzi, M., Cappellari, M., et al. 2013, *MNRAS*, 430, 1219

Pinna, F., Falcón-Barroso, J., Martig, M., et al. 2019a, *A&A*, 625, A95  
 Pinna, F., Falcón-Barroso, J., Martig, M., et al. 2019b, *A&A*, 623, A19  
 Reid, W. A. & Parker, Q. A. 2010, *MNRAS*, 405, 1349  
 Romanowsky, A. J., Douglas, N. G., Kuijken, K., et al. 2003, in *Bulletin of the American Astronomical Society*, Vol. 35, *American Astronomical Society Meeting Abstracts*, 1312  
 Rose, W. K. & Smith, R. L. 1970, *The Astrophysical Journal*, 159, 903  
 Rosenfield, P., Johnson, L. C., Girardi, L., et al. 2012, *ApJ*, 755, 131  
 Sarzi, M., Falcón-Barroso, J., Davies, R. L., et al. 2006, *MNRAS*, 366, 1151  
 Sarzi, M., Iodice, E., Coccato, L., et al. 2018, *A&A*, 616, A121  
 Sarzi, M., Mamon, G. A., Cappellari, M., et al. 2011, *MNRAS*, 415, 2832  
 Spriggs, T. W., Sarzi, M., Napiwotzki, R., et al. 2020, *A&A*, 637, A62  
 Torres, G. 2010, *The Astronomical Journal*, 140, 1158  
 Valenzuela, L. M., Méndez, R. H., & Miller Bertolami, M. M. 2019, *ApJ*, 887, 65  
 Vazdekis, A., Koleva, M., Ricciardelli, E., Röck, B., & Falcón-Barroso, J. 2016, *MNRAS*, 463, 3409  
 Ventimiglia, G., Arnaboldi, M., & Gerhard, O. 2011, *A&A*, 528, A24  
 Weijmans, A.-M., Cappellari, M., Bacon, R., et al. 2009, *MNRAS*, 398, 561  
 Weilbacher, P. M., Streicher, O., Urrutia, T., et al. 2012, in *Society of Photo-Optical Instrumentation Engineers (SPIE) Conference Series*, Vol. 8451, *Software and Cyberinfrastructure for Astronomy II*, ed. N. M. Radziwill & G. Chiozzi, 84510B  
 Willmer, C. N. 2018, *The Astrophysical Journal Supplement Series*, 236, 47